Nano-Micro Letters

e-ISSN 2150-5551
CN 31-2103/TB

ARTICLE

https://doi.org/10.1007/s40820-024-01542-x

Cite as
Nano-Micro Lett.
(2025) 17:51

Received: 30 June 2024
Accepted: 23 September 2024

Scalable Ir-Doped $NiFe_2O_4/TiO_2$ Heterojunction Anode for Decentralized Saline Wastewater Treatment and H_2 Production

Sukhwa Hong[1], Jiseon Kim[1], Jaebeom Park[1], Sunmi Im[1], Michael R. Hoffmann[2], Kangwoo Cho[1,2,3] ✉

HIGHLIGHTS

- Ir-doped $NiFe_2O_4$ (NFI) spinel with TiO_2 heterojunction overlayer brought about outstanding chlorine evolution reaction in circum-neutral pH.
- Electroanalyses including operando X-ray absorption spectroscopy uncovered the active role of TiO_2 for Cl^- chemisorption.
- NFI/TiO_2 anode boosted both NH_4^+-to-N_2 conversion and H_2 generation in wastewater, and the practical applicability was confirmed with scaled-up anodes and real wastewater.

ABSTRACT Wastewater electrolysis cells (WECs) for decentralized wastewater treatment/reuse coupled with H_2 production can reduce the carbon footprint associated with transportation of water, waste, and energy carrier. This study reports Ir-doped $NiFe_2O_4$ (NFI, ~ 5 at% Ir) spinel layer with TiO_2 overlayer (NFI/TiO_2), as a scalable heterojunction anode for direct electrolysis of wastewater with circum-neutral pH in a single-compartment cell. In dilute (0.1 M) NaCl solutions, the NFI/TiO_2 marks superior activity and selectivity for chlorine evolution reaction, outperforming the benchmark IrO_2. Robust operation in near-neutral pH was confirmed. Electroanalyses including *operando* X-ray absorption spectroscopy unveiled crucial roles of TiO_2 which serves both as the primary site for Cl^- chemisorption and a protective layer for NFI as an ohmic contact. Galvanostatic electrolysis of NH_4^+-laden synthetic wastewater demonstrated that NFI/TiO_2 not only achieves quasi-stoichiometric NH_4^+-to-N_2 conversion, but also enhances H_2 generation efficiency with minimal competing reactions such as reduction of dissolved oxygen and reactive chlorine. The scaled-up WEC with NFI/TiO_2 was demonstrated for electrolysis of toilet wastewater.

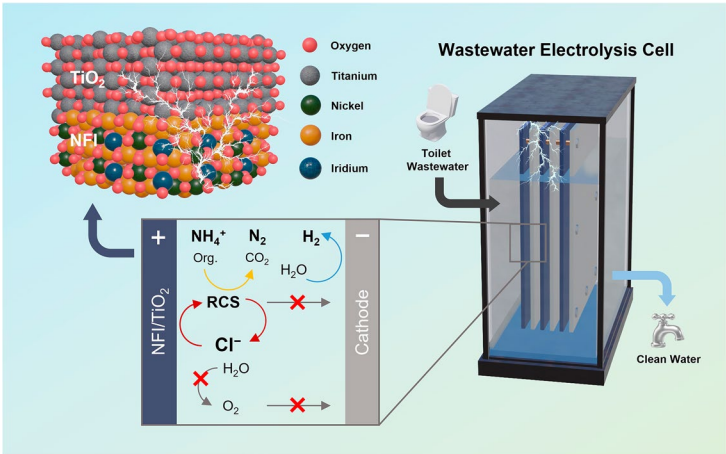

KEYWORDS Wastewater electrolysis cell; Ir-doped $NiFe_2O_4$; Reactive chlorine species; Decentralized H_2 production; On-site wastewater treatment

✉ Kangwoo Cho, kwcho1982@postech.ac.kr
[1] Division of Environmental Science and Engineering, Pohang University of Science and Technology (POSTECH), Pohang 790−784, Korea
[2] Linde Laboratory, California Institute of Technology, Pasadena, CA 91125, USA
[3] Institute for Convergence Research and Education in Advanced Technology (I-CREATE), Yonsei University International Campus, Incheon 21983, Republic of Korea

Published online: 28 October 2024

Abbreviations

EOP	Electrochemical oxidation process
ClER	Chlorine evolution reaction
RCS	Reactive chlorine species
WECs	Wastewater electrolysis cells
HER	Hydrogen evolution reaction
BDD	Boron-doped diamond
OER	Oxygen evolution reaction
NF	$NiFe_2O_4$
NFI	Ir-doped $NiFe_2O_4$
FE-SEM	Field emission scanning electron microscope
EDS	Energy-dispersive X-ray spectrometer
XRF	X-ray fluorescence
XRD	X-ray diffraction
XPS	X-ray photoelectron spectroscopy
PAL	Pohang accelerate laboratory
XANES	X-ray absorption near-edge structure
OCV	Open circuit voltage
CI	Current interruption
CV	Cyclic voltammetry
LSV	Linear sweep voltammetry
CDL	Double-layer capacitance
ECSA	Electrochemically active surface area
EIS	Electrochemical impedance spectroscopy
R_s	Solution resistance
R_f	Films resistance
R_{ct}	Charge transfer resistance
PZC	Potential of zero charge
M-S	Mott–Schottky
DPD	N,N-diethyl-p-phenylenediamine
HHV	Higher heating value
TN	Total nitrogen
COD	Chemical oxygen demand
IC	Ion chromatography
GC-TCD	Gas chromatography with thermal conductivity detector
EEM	Excitation-emission matrix
DOM	Dissolved organic matter
RHE	Reversible hydrogen electrode
CE	Current efficiency
EE	Energy efficiency
TOC	Total organic carbon

1 Introduction

The current societal pursuit toward carbon neutrality would necessitate self-contained systems, ultimately to be independent on the existing water and energy grid. For example, on-site wastewater treatment and reuse are beneficial for a sustainable water cycle in adaptation to the climate change [1]. In addition, a reduction in water and waste transportation would decrease the carbon footprint [2] for sanitation and hygiene to meet the Sustainability Development Goals established by the United Nations. To this end, electrochemical oxidation processes (EOPs) have emerged as a promising way of decentralized treatment of toilet wastewater and effluent reuse [3]. While achieving adequate effluent level set by the International Organization for Standardization (*e.g.*, ISO 30500 [4]), the EOPs could be advantageous with respect to ease of automation and connection with renewable energy sources (*e.g.*, using photovoltaic panels) [5]. A long-term operation of a combined anaerobic digester and EOP has been demonstrated for a self-contained public toilet with a nonpotable water reuse (flushing) [6].

The chlorine evolution reaction (ClER) on electrocatalysts oxidizes chloride ion to reactive chlorine species (RCS), the core mediator to degrade aqueous organic pollutants and ammonium (NH_4^+) [7–9]. In particular, the efficient deammonification by the electrolytic RCS has been a subject of significant attention [10–12], which has been rarely achieved by conventional septic systems or other non-sewered sanitation systems based on biological (de)nitrification, stripping, ion exchange, and wet chemical treatments [10, 13]. Almost stoichiometric conversion of NH_4^+ to N_2 by the *in situ* generated RCS without a generation of N-containing greenhouse gases (*e.g.*, N_2O, NH_3) should be environmentally sustainable, while alleviating concerns related to NH_4^+ such as eutrophication and odors.

On the other hand, a distributed electrolysis of nontraditional water sources including wastewater (effluent) can be involved within the H_2 economy [14]. A local production of deionized water by reverse osmosis is known to contribute marginally to the overall H_2 production cost by electrolysis. However, it can compete with drinking water production in the areas with surplus renewable energy (*e.g.*, desert). In this regard, contributions from Hoffmann and coworkers [15] advocate wastewater electrolysis cells (WECs) for localized conversion of renewable energy into H_2, reducing the costs and CO_2 emission for (waste) water treatment and transportation. A usage of separator (*e.g.*, proton exchange membrane) in a direct wastewater electrolysis could bring about proliferating ohmic losses and

https://doi.org/10.1007/s40820-024-01542-x

contamination of the separator in wastewater matrix. In the single-compartment WEC, therefore, oxygen reduction reaction competes with the hydrogen evolution reaction (HER), substantially decreasing the current and energy efficiency [15]. Relatively low-grade H_2 (< 60%) in mixture with N_2 (from deammonification) and CO_2 (from mineralization) can be utilized by combustion, in a decent analogy with the existing chloralkali processes that generates H_2 as a byproduct. This approach might be more available and appropriate practice.

Nonetheless, the bottlenecks of WEC include requirements of precious element-based electrocatalysts and unsatisfactory selectivity of ClER. The current anode materials in EOPs exclusively rely on dimensional stable anode (DSA; $IrTaO_x$ and $RuTiO_x$) [16, 17] and boron-doped diamond (BDD) [18], unaffordable for a decentralized system. In spite of the recent developments on electrocatalysts based on earth-abundant elements (*e.g.*, Ni, Fe, Co, Cu, Zn, Mo among others) [19–23], their instability in near-neutral pH required an alkalified wastewater, while inferior ClER selectivity with dominant oxygen evolution reaction (OER) ruled out a concurrent pollutants degradation during the electrolysis [24]. To this end, evidences have been presented that TiO_2 outer layers in heterojunction with conductive Ir-based DSA could enhance both the ClER selectivity and durability [7–9], although the underlying mechanism remains ambiguous. In addition, we recently reported $NiFe_2O_4$ (NF) electrocatalysts with a tiny amount (5 mol%) of Ir doping (NFI) could enable extraordinary OER activity and stability [25]. A scaling relation between OER and ClER on (mixed) metal oxide electrocatalysts motivated us to further deploy the NFI for ClER in circumneutral pH in combination with the TiO_2 heterojunction layer.

Within the aforementioned context, this study reports that NFI/TiO_2 heterojunction anode (prepared by a straightforward solution casting) allows ClER activity superior to the benchmark IrO_2 and almost absolute ClER selectivity in 0.1 M NaCl solutions. Electrolysis of NH_4^+-laden synthetic wastewater demonstrated that the admirable ClER metrics simultaneously enhanced the kinetics of pollutants degradation and H_2 generation. Electroanalyses coupled with *operando* X-ray absorption spectroscopy revealed active ClER primarily on TiO_2, while the underlying NFI served as an ohmic contact. The practical applicability was validated by a scaled-up WEC with toilet wastewater.

2 Experimental Section

2.1 Preparation of NFI/TiO_2 Anode

Ti foils (Alfa Aesar, 3×1 cm^2, 0.25 mm thick, 99.5% purity) underwent pretreatments to remove impurities, including SiC sandblasting, degreasing by ultrasonication in a mixed solvent (with equal volumes of ethanol, acetone, and deionized (DI) water (18.2 MΩ, Millipore)) for 0.5 h, and immersion in 10 wt% boiling oxalic acid for 0.5 h. The precursors for mixed Ni–Fe oxides were prepared using nitrate salts ($Ni(NO_3)_2{\cdot}6H_2O$ and $Fe(NO_3)_3{\cdot}9H_2O$, both from Alfa Aesar in 99% purity) dissolved in DI water with 0.1 M urea, in variable molar ratios of Ni to Fe ([total metal] = 250 mM). In particular, the precursor with Ni-to-Fe ratio of 1:2 was used for NF. For IrO_2 preparation, 250 mM H_2IrCl_6 was dissolved in a mixed solution with equi-volumes of ethanol, isopropanol, and 0.3 M HCl. A calculated amount of the Ir-precursor was added to the NF precursor ([Ir] = 12 mM) for the NFI. Ti-glycolate precursor for TiO_2 layer was prepared by a peroxo-method [7, 26]. In short, 0.25 M $Ti(C_4H_9O)_4$ was dissolved in 0.4 M glycolic acid solution by addition of concentrated H_2O_2, and the final pH was adjusted to be circumneutral by addition of concentrated NH_4OH. All anodes interrogated in this study were fabricated by drop-casting (1 μL cm^{-2}), drying for 15 min (80 °C), and annealing for 15 min (425 °C for NF, NFI, and TiO_2; 525 °C for IrO_2). This sequence was repeated up to total 6 coats which underwent final annealing for 1.5 h (Fig. 1a). A commercial BDD electrode as a control was provided by Wesco Electrode.

2.2 Anode Characterization

The surface morphology was observed by high-resolution field emission scanning electron microscope (FE-SEM, JSM 7800F PRIME). The elemental compositions were estimated by energy-dispersive X-ray spectrometer (EDS, LN2 Free SDD type) with FE-SEM, X-ray fluorescence (ED-XRF, SII Nano technology Inc., SEA1200VX), and glow discharge spectrometry (GDS, LECO GDS850A with Radio Frequency Lamp). The crystalline structure was analyzed by X-ray diffraction (XRD, Phillips X'Pert Panalytical diffractometer) at 30 mA, 40 kV, and

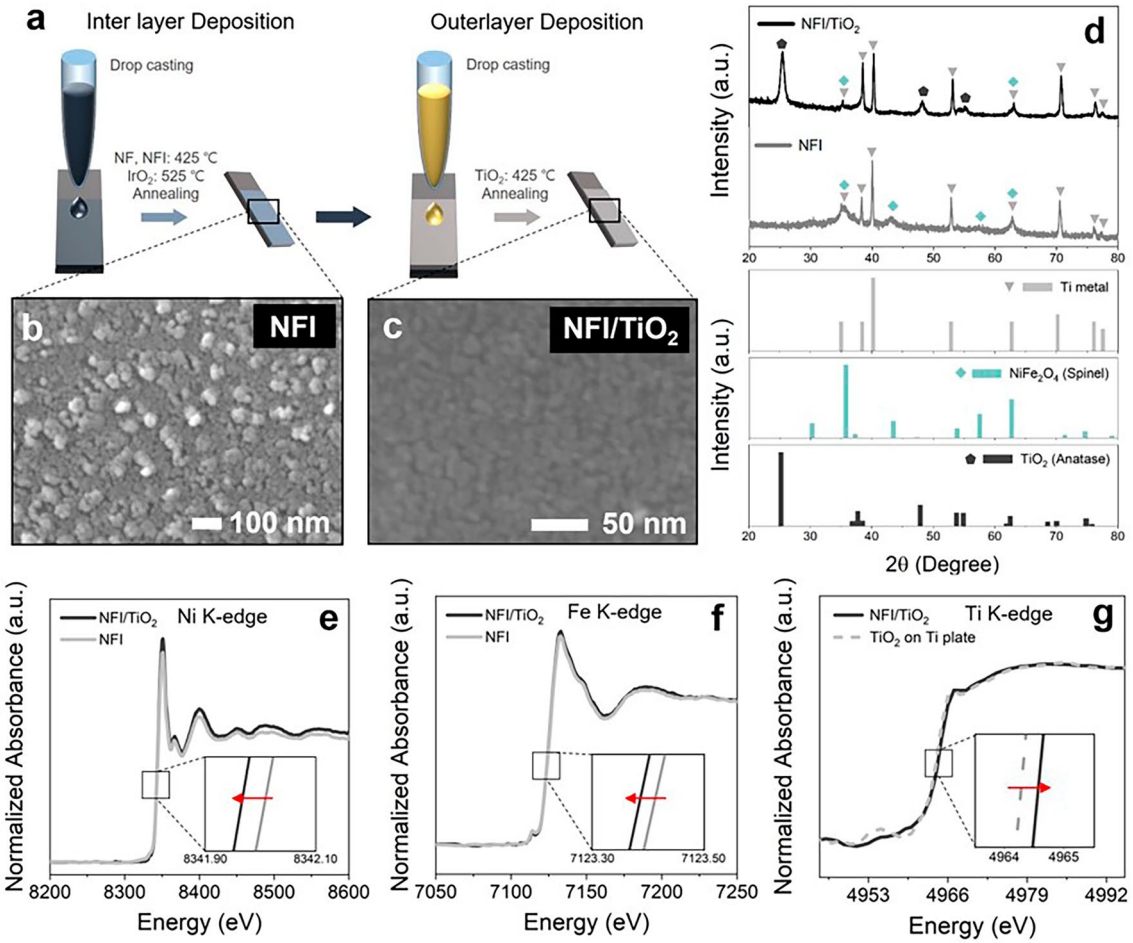

Fig. 1 Preparation and characterization of NFI/TiO_2 anode. **a** Schematic illustration of the synthesis procedure. **b-c** Horizontal SEM images of NFI and NFI/TiO_2. **d** XRD profiles of NFI and NFI/TiO_2 with references. **e–g** *Ex situ* XANES for Ni K-edge, Fe K-edge, and Ti K-edge of NFI/TiO_2 in comparison with NFI or Ti/TiO_2

monochromated Cu Kα1 radiation. Raman spectra were collected by Alpha 300R (WITec) with a × 50 objective and wavelength of 488 nm using an Ar^+ excitation source. The composition and oxidation states on surface (up to ~ 10 nm) were investigated by K-ALPHA X-ray photoelectron spectroscopy (XPS, Thermo Fisher Scientific, UK) using a monochromated Al Kα (12 kV, 72 W, 1486.6 eV, 400 μm spot size). The bulk electronic structure was interrogated by X-ray absorption spectroscopy at the 10C beamline in Pohang Accelerate Laboratory (PAL), to give X-ray absorption near-edge structure (XANES) spectra. *operando* XANES analysis proceeded with the working electrode attached to the cell window by Kapton tape, under open circuit voltage (OCV), pre-ClER, and ClER condition at a minute interval.

2.3 Electroanalysis

A single-compartment cell (working volume: 35 mL) was used with three-electrode configuration including an anode under investigation (effective geometric area: 2 × 1 cm^2), a Pt coil cathode (BASi), and a reference electrode. Ag/AgCl (BASi) and Hg/HgO (BASi) reference electrodes were used for electrolyte with neutral and alkaline pH, respectively. The spacing between the working and counter electrode was maintained at 0.5 cm. The measured potentials were converted to RHE scale by $E_{RHE} = E_{Ag/AgCl} + 0.197 + 0.059 \times pH = E_{Hg/HgO} + 0.140 + 0.059 \times pH$. The working electrode potential (E_{we}) was compensated with ohmic (iR) drop, based on a current interruption (CI) method at 85% level. The electrochemical activity and stability were

https://doi.org/10.1007/s40820-024-01542-x

evaluated based on cyclic voltammetry (CV), linear sweep voltammetry (LSV), and chronopotentiometry using a potentiostat (VSP, BioLogic). Double-layer capacitance (C_{DL}), which represents the electrochemically active surface area (ECSA), was measured by CV in a non-Faradaic potential window at variable scan rates (1 to 100 mV s^{-1}) in 0.1 M NaCl (j_a–j_c at 0.861 V_{RHE}) and 1 M KOH (j_a–j_c at 1.17 V_{RHE}). The electrochemical impedance spectroscopy (EIS) estimated solution resistance (R_s), films resistance (R_f), and charge transfer resistance (R_{ct}), with fitting by EC − Lab software (VSP, BioLogic). The baseline potential for EIS was 1.3 V Ag/AgCl in 0.1 M NaCl, while the sinus amplitude of 10 mV and frequency scan range of 100 kHz to 100 mHz were used. The potential of zero charge (PZC) was determined based on the potential where the capacitance was minimized [27]. The changes in capacitance at different potentials were tracked using EIS operated through a potentiostat (VSP, BioLogic). These impedance measurements, which varied with the applied potential, were taken in 0.05 M NaCl solutions, using a frequency of 150 mHz and a sinus amplitude of 5 mV. By applying 6th-order polynomial fitting to the spectra, the point where F was at its minimum was established as the PZC [27]. The Mott–Schottky (M-S) plots were obtained by EIS (sinus amplitude: 10 mV, frequency range: 10 kHz to 10 Hz, and potential range: 0 to 1 V versus reference electrode). The M-S slope from the following equation was used to comparatively evaluate the electrical conductivity [28, 29]:

$$\frac{1}{C_{sc}^2} = \left(\frac{2}{\varepsilon\varepsilon_0 e A^2 N_d}\right)\left[\left(E_{we} - E_{FB}\right) - \frac{kT}{e}\right] \quad (1)$$

where C_{SC} is the space charge capacitance (F), ε is the dielectric constant, ε_0 is the permittivity of the vacuum (8.854×10^{-12} F m^{-1}), e is the elementary charge (1.602×10^{-19} C), N_d is donor density (m^{-3}), A is active surface area (m^2), E_{we} is the applied potential to the working electrode (V), E_{FB} is the flat band potential (V), k is Boltzmann's constant (8.62×10^{-5} eV K^{-1}), and T is the absolute temperature (K). Prior to all electroanalyses, the cell was rested in open circuit for 15 min.

2.4 RCS Generation by Galvanostatic Bulk Electrolysis

The ClER in aqueous electrolyte generates free chlorine species including HOCl and OCl^- by pH-dependent hydrolysis of Cl_2 [10]. The performance of ClER (RCS generation) was evaluated by galvanostatic electrolysis of 0.1 M NaCl solutions at variable current density (j, 10 to 50 mA cm^{-2}). The evolution of [RCS] was periodically quantified with DPD reagents for initial 7 min, where ClO_3^- or ClO_4^- generations were negligible. This study used the following metrics for fair comparison of anodes [7, 8]. The CE_{ClER}, EE_{ClER}, and SR_{ClER} of ClER were estimated by the equations below [7, 8]:

$$\text{CEClER}\ (\%) = \frac{2VFd[RCS]}{jAdt} \quad (2)$$

$$EE_{ClER}\left(\text{mmol Wh}^{-1}\right) = \frac{Vd[RCS]}{E_c jAdt} \times 3.6 \times 10^6 \quad (3)$$

$$SR_{ClER}(\text{mmol cm}^{-2}\text{h}^{-1}) = \frac{\text{V d[RCS]}}{\text{A dt}} \times 360 \quad (4)$$

where V represents the volume of the electrolyte (0.035 L), F is Faraday constant (96,485.3 C mol^{-1}), d[RCS]/dt is RCS generation rate (M s^{-1}), j is current density (A m^{-2}), t is electrolysis time (s), and E_c is cell voltage (V).

2.5 RCS-Mediated Wastewater Treatment Coupled with H_2 Generation

Using the aforementioned cell, bulk galvanostatic (30 mA cm^{-2}) electrolysis experiments for RCS-mediated conversion of NH_4^+ to N_2 with simultaneous HER proceeded in synthetic wastewater samples. The $[Cl^-]_0$ was fixed at 0.1 M, while $[NH_4^+]_0$ was varied ($[NH_4^+]_0$:$[Cl^-]_0$ = 2:1, 1.5:1, 1:1, 1:1.5, 1:2, 1:3, and 1:4 in molar basis) by mixing NH_4Cl, NaCl, and $(NH_4)_2SO_4$. The CE of pollutants oxidation as well as CE and EE for HER were estimated by following equations [15]:

$$CE(\text{pollutants oxidation}) = \frac{nVFdC}{jAdt} \quad (5)$$

$$CE_{HER} = \frac{2\,F\,Q}{j\,\text{A}} \quad (6)$$

$$EE_{HER} = \frac{HHV\,Q}{E_c\,j\,A} \quad (7)$$

where n is the number of electron transfer for oxidation of aqueous pollutants (3 for NH_4^+-to-N_2 conversion), dC/dt is decreased pollutants concentration per unit electrolysis time of t (M s^{-1}), Q is the observed H_2 production rate (mol s^{-1}), and HHV is higher heating value of H_2 (78 Wh mol^{-1}).

To demonstrate practical applicability, a pilot-scale WEC was manufactured in working volume of 10 L (with internal circulation). Scaled-up NFI/TiO_2 anodes and commercial stainless steel 304 cathode were prepared in size of 35.8×26.6 cm^2. Three anodes and cathodes were alternately sandwiched (with inter-electrodes distance of 1 cm) and connected to a power supply (ODA Tech, EX30-60) in monopolar configuration. The geometric surface area of the electrode module exposed to electrolyte was 0.191 m^2. Toilet wastewater was mimicked by mixing livestock excretion (collected from Gyungju wastewater treatment plant, Korea), seawater (collected in Pohang, Korea), and tap water by volume ratio of 5:20:75. The composition of the toilet wastewater was summarized with 102 mgN L^{-1} of NH_4^+, 104 mgN L^{-1} of total nitrogen (TN), 580 mgO_2 L^{-1} of chemical oxygen demand (COD), 120 NTU of turbidity, 121 mM of Cl^-, 7.9 of pH, and 14.7 mS cm^{-1} of conductivity. The wastewater sample was subjected to electrolysis at constant current of 52.5 A (corresponding to 27.5 mA cm^{-2}) for 3 h.

Quantification of anions (*e.g.*, Cl^-, ClO_3^-, NO_2^-, and NO_3^-) was carried out by ion chromatography (IC, DX-120). The concentration of free chlorine and total chlorine were measured using DPD (N,N-diethyl-p-phenylenediamine) and DPD/KI reagents, respectively, based on absorbance at 530 nm in UV–Vis spectrometer (DR 3900, HACH). Combined chlorine (e.g., chloramines) was estimated from the difference between free chlorine and total chlorine [30]. TN was quantified using alkaline persulfate digestion [31] based on absorbance of nitrate at 420 nm. NH_3-N was analyzed by salicylate method with commercial kits (NH_3-N TNT kit, HACH) and absorbance at 610 nm [32]. [COD] was measured by dichromate digestion with colorimetric detection at 348 nm [33]. Gaseous H_2, N_2, and O_2 in reactor headspace were streamed with carrier Ar gas to pass through a gas flow meter (Ritter MilliGascounter), and the composition was measured by gas chromatography with thermal conductivity detector (GC-TCD, 6890-N, Agilent Technologies). Turbidity of toilet wastewater was measured using turbidity colorimeter (HUMAS, TURBY 1000). The excitation-emission matrix (EEM) with fluorescence spectrometer (FluoroMax-4) was collected to qualitatively investigate the variations in dissolved organic matter (DOM).

3 Results and Discussion

3.1 Characterization of NFI/TiO_2 Heterojunction Anode

The NFI/TiO_2 anodes were fabricated through a straightforward drop-casting method (Fig. 1a). The horizontal images of FE-SEM discovered NFI nanoparticles sized in the range of 50–100 nm (Fig. 1b) which aggregated during the thermal treatment to bring about tableland and ridge morphology on the Ti substrate, as shown by EDS mapping (Fig. S1). The M-edge signals of Ir and K-edge signals of Ni, Fe, Ti, and O revealed even elemental distributions on the NFI aggregates. The EDS-based molar fraction of Ir was 5.27% for NFI, in decent agreement with 5.15% from ED-XRF analysis (Fig. S2). These values close to the precursor composition (5%) suggested homogeneous Ir doping on NFI. XRD patterns of NF and NFI powders (physically abraded from the Ti substrate) confirmed that the $NiFe_2O_4$ spinel crystalline lattice (JCPDS No. 10–0325, $2\theta = 36°$, 43°, and 63° corresponding to (311), (400), and (440)) [25] of NF was retained for NFI despite the Ir dopants (Fig. S3a). Raman spectra for NF and NFI (Fig. S3b) both exhibited congruence with the $NiFe_2O_4$ spinel structure of space group Fd-3 m, as affirmed with active bands including A_{1g} (symmetric stretch), E_g (symmetric bend), and T_{2g} (asymmetric stretch) for tetrahedral and octahedral sites [34]. This evidence substantiated the uniform doping of Ir into NF nanoparticles without insignificant structural perturbation and segregation into IrO_2.

The SEM/EDS analysis on NFI/TiO_2 noticed a stacked film of TiO_2 nanoparticles sized by 10–20 nm (Fig. 1c), to allow more even deposition of TiO_2 outer layer reducing surface tortuosity (Fig. S4). The nanoporous property of the TiO_2 layer would allow diffusive penetration of reactants such as H_2O, OH^-, and Cl^- [26]. The XRD patterns of NFI and NFI/TiO_2 electrodes (Fig. 1d) were dominated by signals from the Ti metal substrate (JCPDS No. 44–1294, $2\theta = 35°$, 38°, 40°, 52°, 62°, 70°, 76°, and 77°) that largely overlapped with those of spinel $NiFe_2O_4$ peaks. NFI/TiO_2 showed additional diffraction peaks from anatase TiO_2 (JCPDS No. 21–1272, $2\theta = 25°$ and 48° corresponding to (101) and (200), respectively). These evidences characterized the NFI/TiO_2 as Ir-doped $NiFe_2O_4$ in heterojunction with nanoporous TiO_2 layer. A GDS analysis (Fig. S5)

https://doi.org/10.1007/s40820-024-01542-x

estimated the thickness of TiO_2 and NFI to be ~ 250 nm and ~ 2.75 μm, respectively.

XPS for NF and NFI (Fig. S6) clarified partial charge transfer from Ni and Fe to the Ir dopants. The fractions of Ni^{3+} and Fe^{3+} from deconvoluted Ni $2p_{3/2}$ (854.5 eV for Ni^{2+} and 856 eV for Ni^{3+} with two satellite peaks at 861 and 865 eV) [35] and Fe $2p_{3/2}$ [36] (710 eV for $Fe^{2+}$and 711.5 eV for Fe^{3+}) photoelectron spectra were elevated in NFI, whereas the binding energy of Ir 4*f* peak was between those of Ir^{4+} (61.8 eV) and Ir^0 (60.9 eV) [37]. The deconvolution of O 1*s* spectra noted escalated fraction of oxygen vacancy upon the Ir doping. These observations were in agreement with the prior report on NFI coated on Ni foam [25]. On the other hand, the Ti 2*p* photoelectron spectra for NF/TiO_2 and NFI/TiO_2 both indicated a partial oxidation of Ti (Fig. S7), in comparison with the TiO_2 layers directly coated on the Ti substrate (Ti/TiO_2). However, the concurrent shifts in electronic structure of the underlying layers were intangible due to the limited analytical depth of XPS. To this end, XANES unambiguously informed on the electronic interaction across the heterojunction, based on the edge position of individual metal components at the half-maximum intensity to represent the oxidation state. The Ti K-edge position of NFI/TiO_2 was positively shifted compared to Ti/TiO_2 (Fig. 1f), whereas both Ni and Fe K-edge region absorbance spectra for NFI/TiO_2 suggested decreased valency compared to NFI (Fig. 1e, f). The *ex situ* XANES thus provides compelling evidence of charge transfer from the outer TiO_2 to the underlying NFI across the interface.

3.2 Electrocatalytic Behaviors of NFI/TiO_2 Heterojunction Anode

Given the scaling relation between OER and ClER intermediates for (mixed) metal oxide electrocatalysts [38], screening electrocatalysts in terms of OER activity could be a precedent step to employ the OER intermediates as ClER center [26]. Due to a composition-dependent instability of $Ni_xFe_{1-x}O_y$ electrocatalysts in acidic-to-neutral pH, moreover, it was inevitable to evaluate them in alkaline electrolyte where OER would overwhelm ClER. LSV curves in 1 M KOH confirmed extraordinary OER activity of $NiFe_2O_4$ spinel oxide substantially outperforming the other $Ni_xFe_{1-x}O_y$ compositions (x = 0, 0.2, 0.5, 0.67, 0.8, and 1) identically synthesized by dip coating (Fig. S8) [26, 39]. Mixing Ir within the $NiFe_2O_4$ precursor at variable atomic ratio (0, 1%, 3%, 5%, 7%, and 10%) enhanced OER activity up to 5% Ir on the modified electrocatalysts, judging from overpotential (η) at 10 mA cm^{-2} (Fig. S9). Further elevation in Ir contents marginally influenced the current wave, in compatible with the previous report [25].

Armed with the supreme OER activity of NFI (5% Ir-doped $NiFe_2O_4$), the electrochemical performances of NFI and NFI/TiO_2 were assessed in 0.1 M NaCl electrolyte with circumneutral pH, and compared with NF and IrO_2 with or without the TiO_2 overlayer. It should be noted that ClER and OER would occur in parallel in this experimental condition. The XRD for the control group samples confirmed crystallinity of spinel $NiFe_2O_4$, rutile IrO_2 (JCPDS No. 15–870), and anatase TiO_2. (Fig. S10). The voltammograms (Fig. 2a) estimated required potentials at 10 mA cm^{-2} to be 2.00, 2.07, 1.81, 1.83, 1.88, and 1.90 V versus reversible hydrogen electrode (RHE) for NF, NF/TiO_2, NFI, NFI/TiO_2, IrO_2, and IrO_2/TiO_2, respectively. The NFI exhibited the most facile charge transfer kinetics, even outperforming the benchmarked IrO_2. Although the TiO_2 overlayer moderately lowered the anodic wave, NFI/TiO_2 still marked superior activity compared to the IrO_2. The C_{DL} was measured by plotting charging current density ($j_a - j_c$) as linear functions of scan rate (Figs. 2b and S11). The C_{DL} value, as a surrogate of ECSA, showed analogous trend with the LSV. Nyquist plot from EIS disentangled R_f and R_{ct} [40], as shown in Fig. S12. The IrO_2 exhibited singular semicircle owing to the conductor-like property, whereas the R_f was noted for NF and NFI by additional semicircles in lower frequency ranges. The R_{ct} based on diameter of the higher frequency semicircles agreed with the activity trends, while the TiO_2 overlayers substantially increased the R_f for the heterojunction anodes. Therefore, the moderate current reduction by the TiO_2 layer was ascribed to resistance to charge migration (due to an inferior electrical conductivity of TiO_2) and/or pore diffusion through the nanoporous film that was incompletely compensated by the CI method.

The overall activity trends were maintained in voltammograms obtained in 1 M KOH (Fig. S13), because of the scaling relation between adsorption energy for intermediates of OER (*OOH) and ClER (*OCl) on metal oxide electrocatalysts [7, 8]. The OER η of NFI (330 mV) at 10 mA cm^{-2} was lower than NF and IrO_2. We previously presented evidences that Ir doping on $NiFe_2O_4$ could shift the active motif from Fe–O–Fe to Ni–O–Fe to concurrently escalate ECSA

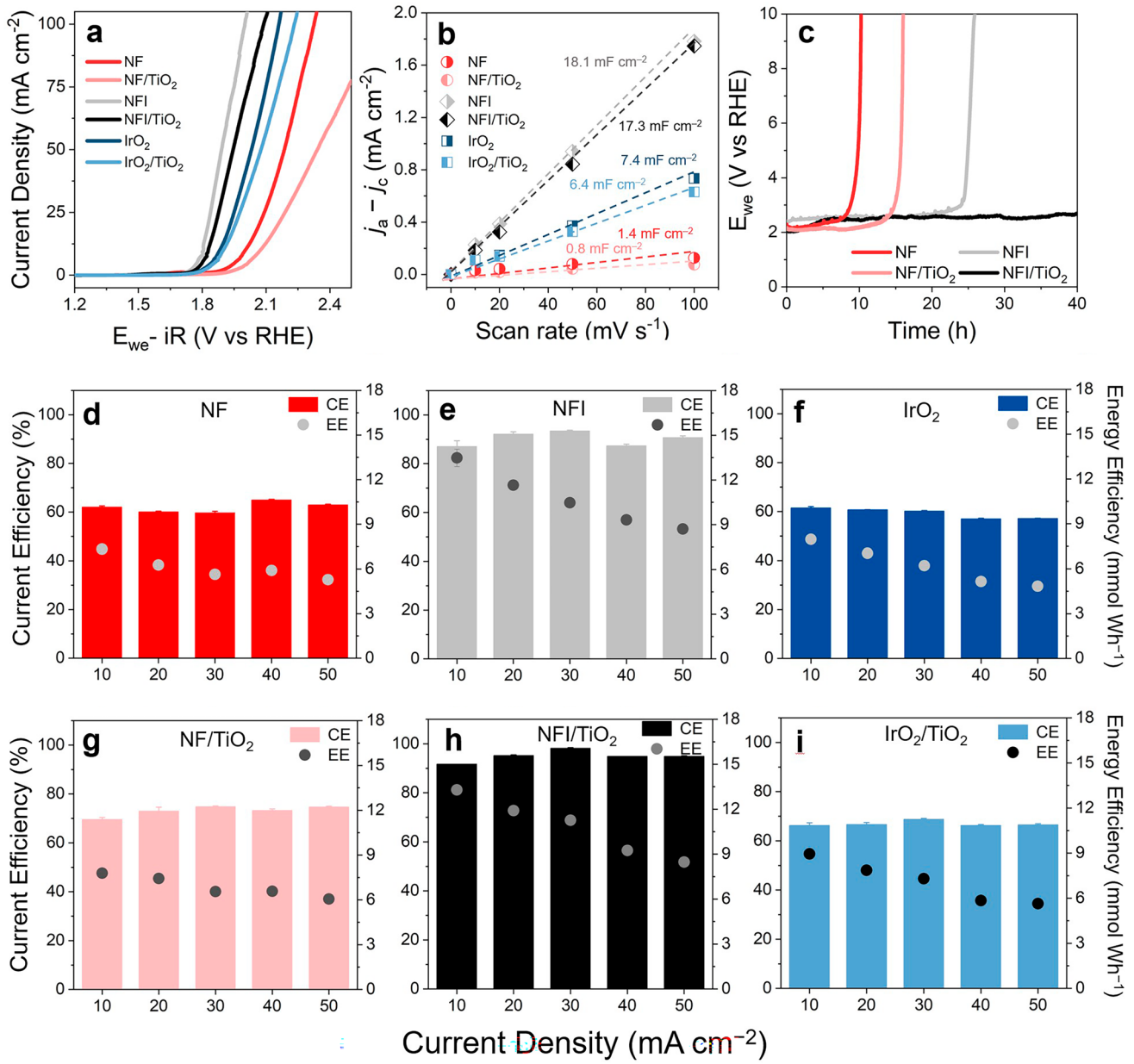

Fig. 2 Electrochemical performances. **a** LSV curves (scan rate: 10 mV s^{-1}) with 85% *iR* correction. **b** Capacitive j_a–j_c versus scan rate from CV (potential range: 0–0.5 V vs. Ag/AgCl, scan rate: 10, 20, 50, and 100 mV s^{-1}) for NFI, NFI/TiO_2, NF, NF/TiO, IrO_2, and IrO_2/TiO_2 electrocatalysts in 100 mM NaCl. **c** Chrono-potentiometric profile for long-term stability test of NFI, NFI/TiO_2, NF, NF/TiO_2 in 0.5 M $NaClO_4$. **d-i** CE_{ClER} and EE_{ClER} during galvanostatic electrolysis of 0.1 M NaCl solutions for NF, NFI IrO_2, NF/TiO_2, NFI/TiO_2, and IrO_2/TiO_2

and intrinsic OER activity of NF [25]. If the porous TiO_2 layers were electrochemically inert, on the other hand, the reduction of ECSA by the TiO_2 deposition would be independent on the electrolyte while the mass transport resistance through the TiO_2 film could be alleviated in 1 M KOH. However, the TiO_2 layer reduced the C_{DL} value (Fig. S14) of NFI more significantly in 1 M KOH compared to those in 0.1 M NaCl. It implicitly elucidated an active electrocatalytic roles of TiO_2 for ClER. Mott–Schottky slopes both in 1 M KOH and 0.1 M NaCl (Fig. S15) further revealed substantially elevated donor density and electrical conductivity for NFI, compared to NF. The observed p-type property of $NiFe_2O_4$ [41] rationalized the electron withdrawing from the TiO_2 (well-known n-type semiconductor) through

https://doi.org/10.1007/s40820-024-01542-x

p-n heterojunction (Fig. S7) [42, 43]. The superior conductivity of NFI should be advantageous as an ohmic contact to reduce the energy barrier for charge transfer from TiO_2 under a forward bias on the anode.

The anodic bias coupled with the generations of RCS and protons in the anode vicinity would cause dissolutions of Ni and Fe [44, 45], which could be accelerated as bulk pH decreases. The long-term stability tests were performed in 0.5 M $NaClO_4$ solution (pH ~ 7) under 30 mA cm^{-2}, where the durability of NFI/TiO_2 (in terms of potential variation over 40 h) clearly outperformed NFI, NF and NF/TiO_2 (Fig. 2c). Repetitive CV further demonstrated the superior stability of NFI/TiO_2 with negligible activity loss during 100 cycles, compared to NF/TiO_2 (Fig. S16). Judging from the well-known stability of TiO_2 in wide potential and pH windows in Pourbaix diagram [46], the varied durability depending on the underlying layer demonstrated penetration of electrolyte through pores and pinholes of the TiO_2 layer. An adsorbate evolution mechanism prevalent on NF and NFI was reported to allow greater service life than other $Ni_xFe_{1-x}O_y$ electrocatalysts based on lattice oxygen mediated mechanism, while the Ir dopants could further increase the required energy for atomic defect formation (dissolution) [25]. In addition, the TiO_2 overlayer could alleviate the diffusion of dissolved components from the buried NF or NFI toward the bulk phase, further reinforcing the stability [26].

The figures-of-merit for ClER were comparatively evaluated in 0.1 M NaCl solutions (Fig. 2d-i) at various current densities (10 to 50 mA cm^{-2}). The galvanostatic regime has been widely deployed for industrial processes owing to more straightforward scaling-up and process control than potentiostatic one. In this condition, the specific ClER rate (SR_{ClER}, Fig. S17) was merely proportional to current efficiency (CE_{ClER}). The CE_{ClER}, the core metric of ClER selectivity, was insignificantly influenced by the applied current densities in this experimental range. This is presumably due to a lack of diffusion limitation for Cl^-, which would allow a flexible operation of EOPs upon a fluctuation of influent wastewater. The average of CE_{ClER} of NF, NF/TiO_2, NFI, NFI/TiO_2, IrO_2, and IrO_2/TiO_2 was calculated to be 61.9%, 73.1%, 90.2%, 95.0%, 59.3%, and 66.9%, respectively (Fig. S18). The NFI itself marked CE_{ClER} exceeded 90% which was further increased by TiO_2. Comparably inferior ClER selectivity of NF and IrO_2 (~ 60% of CE_{ClER}) was evidently improved by the TiO_2 overlayers, in agreement with the previous reports [7, 8, 26]. The exhibited selectivity trend would be associated with surface properties such as O-binding strength [38]. This conjecture was interrogated using PZC, an experimental descriptor for the surface charge density [27]. Specifically, the greater PZC would correspond to the less propensity to lose electron and the lower bond strength with electrophilic *O [47]. A recent theoretical study claimed a fair correlation between the PZC and binding energy of *OH [48]. Figure S19 portrays a weak positive relation between PZC (raw data for PZC determination in Fig. S20) and CE_{ClER}. The influences of specific adsorption and space charge capacitance would account for the deviations from an ideal linearity. The Ir doping on NF substantially elevated the PZC of NFI, which conformed to the escalated oxidation states of Ni and Fe in Ni–O–Fe motifs (Fig. S6). In other words, the weakened binding of *OH could facilitate reaction with Cl^-, to rationalize the greater CE_{ClER} than NF. The TiO_2 overlayers further increased the PZC of NF and NFI to account for the moderate enhancement in ClER efficiency. Considering the strong electronic interaction across the junction (Fig. S7), in analogy, this finding also suggested active involvement of TiO_2 for ClER. If the buried NF or NFI served as the primary ClER sites, the charge withdrawing from the TiO_2 overlayer could strengthen the *OH binding to bring about a reduced CE_{ClER}.

The energy efficiency (EE_{ClER}) in terms of molar amount of RCS per unit energy input should depend both on activity (cell voltage at the given j) and selectivity (CE_{ClER}) [7, 26]. Unlike the CE_{ClER}, EE_{ClER} value justly increased for the smaller j (cell voltage). The TiO_2 overlayers gave ambivalent effects on EE_{ClER}, by enhancing CE_{ClER} in trade-off by increasing the ohmic loss and cell voltage. Accordingly, beneficial improvements in EE_{ClER} by the outer TiO_2 layer were noted for NF/TiO_2 and IrO_2/TiO_2, whereas increases in EE_{ClER} for NFI/TiO_2 were limitedly observed only at 20 and 30 mA cm^{-2} due to high ClER selectivity of NFI itself. Consequently, NFI/TiO_2 recorded the supreme ClER performance and stability with respect to all figures-of-merit under the interrogation conditions. The aforementioned electroanalyses collectively demonstrated that a tiny amount of Ir dopants could boost the ECSA, electrical conductivity, and affinity to Cl^- chemisorption. They in-turn contributed to the outstanding intrinsic ClER activity of NFI, as a promising candidate to replace the precious IrO_2 electrocatalysts. The NFI/TiO_2 architecture further enabled more exceptional RCS generation efficacy, while the protective TiO_2 heterojunction

layer played a pivotal role to elongate the durability during ClER in near-neutral pH.

3.3 ClER Mechanism of NFI/TiO_2 Heterojunction Anode

Our prior reports have demonstrated selective ClER in dilute (< 0.1 M) NaCl on dual-layer anodes which comprised of outer TiO_2 layer in heterojunction with either Ir(Ta)O_x or $NiFeO_x$ [7, 8, 26, 49]. Nevertheless, the precise active site for ClER remained equivocal for these anodes. The electroanalyses in this study including the description of CE_{ClER} by PZC suggested active participation of TiO_2 overlayers in the ClER. In order to obtain conclusive evidences regarding the Cl^- adsorption site for NFI/TiO_2, this study utilized *in situ* XANES analysis that is a powerful tool to monitor changes in the valence state of active elements. The spectra were gained under OCV, pre-ClER at 1 mA cm^{-2} (capacitive current region), and ClER at 3 mA cm^{-2}. The relatively low *j* could avoid the noise by Cl_2 gas on the anode surface [25, 50]. Figure 3 represents normalized absorbance signals in Ni, Fe, and Ti K-edge collected from NFI and NFI/TiO_2. The Ni and Fe K-edge position for NFI markedly showed blue shifts (Fig. 3b, c) monotonically along with the elevated bias from OCV to ClER regime, nominating the Ni–O–Fe motif to be the active site [26]. On the contrary, the valency changes for both Ni and Fe on NFI/TiO_2 were relatively insignificant upon the transition from pre-ClER to ClER regime (Fig. 3e, f), whereas a prominent shift of Ti K-edge was clearly observed (Fig. 3d). It clearly unraveled that the upper TiO_2 would serve as the active ClER sites, while the underlying NFI transformed upon the bias (*e.g.*, Ni–Fe oxyhydroxide with elevated electrical conductivity) would function as the ohmic contact for charge migration. The biased hydrated TiO_2 could form surface *OH as the predominant intermediate conducive to the chemisorption of Cl^-. The effective electron withdrawing by NFI across the p–n junction (Fig. S7) would further facilitate the initial discharge of Cl^- (the presumed rate determining step of ClER) on the charge-deficient TiO_2. In addition, the alleviated oxidation of Ni and Fe could rationalize the elongated service life for NFI/TiO_2 (Fig. 2c).

The roles of NFI and TiO_2 in parallel ClER and OER were further elucidated by LSVs performed either in 0.5 M Na_2SO_4 (for exclusive OER) or 0.5 M NaCl (for predominant ClER as indicated by Fig. 3) electrolyte in pH ~ 7. As shown in Fig. S21, the anodic waves for OER (in Na_2SO_4) and ClER (in NaCl) on NFI were comparable up to 100 mA cm^{-2}. The TiO_2 overcoats diminished the activities in both electrolytes, but the *j* values on NFI/TiO_2 in 0.5 M NaCl exceeded those in Na_2SO_4 electrolyte from the onset to 2.1 V RHE. This noteworthy observation also supported alteration of ClER site from NFI to TiO_2 for the heterojunction anode. The superior ClER in relatively low potentials (< 2.1 V RHE) could attribute to favorable binding of Cl^- to TiO_2. Above this potential, however, the ClER on NFI/TiO_2 was more sluggish than the OER due to pronounced diffusion limitation for Cl^- through the TiO_2 film at the elevated *j*. Figure S22 illustrates the CVs in 1 M KOH + 0.1 M $K_3Fe(CN)_6$ solution. The clearly defined reversible redox peaks of $Fe(CN)_6^{3+/2+}$ on NF and NFI were dramatically attenuated with the presence of TiO_2 overlayer, because of a rejected diffusion of the molecular anion through the pores. Therefore, the active TiO_2 for ClER was speculated to be located in the vicinity of the interface with NFI, presumably in association with the strong interaction with NFI presumably by thermal interdiffusion of metallic components across the junction [7].

3.4 Electrochemical Deammonification Coupled with Molecular H_2 Production

The RCS-mediated NH_4^+ degradation experiments by NFI/TiO_2 anode were conducted with varying $[NH_4^+]_0$ (molar ratio of NH_4^+ to Cl^- from 0.25 to 2), at fixed $[Cl^-]_0$ of 0.1 M and *j* of 30 mA cm^{-2}. As depicted in Fig. 4a, the NH_4^+-N conversion followed apparent zero-order kinetics with superimposable rate constants irrespective of $[NH_4^+]_0$ (~ 10 mM h^{-1} on average), in consistent with previous reports [54]. Regardless of the initial ratios, the ammonium removal efficiency (RE) of NH_4^+ was nearly identical to those for TN, indicating that NH_4^+ was predominantly converted to gaseous N_2 (Fig. 4b). Based on the consistent degradation kinetics, the ratio of $[NH_4^+]_0$ to $[Cl^-]_0$ was fixed at 0.24 for further experiments to monitor the dynamic evolutions of reaction intermediate species during the galvanostatic (30 mA cm^{-2}) deammonification for 3 h. The performance of NFI/TiO_2 was compared with IrO_2/TiO_2 and BDD, as benchmark anodes for water treatment. Electrophilic attacks of RCS to ammonia produce chloramines that are eventually transformed to N_2. The mechanism simplified by the following equations is widely known as breakpoint chlorination in water treatment [30].

https://doi.org/10.1007/s40820-024-01542-x

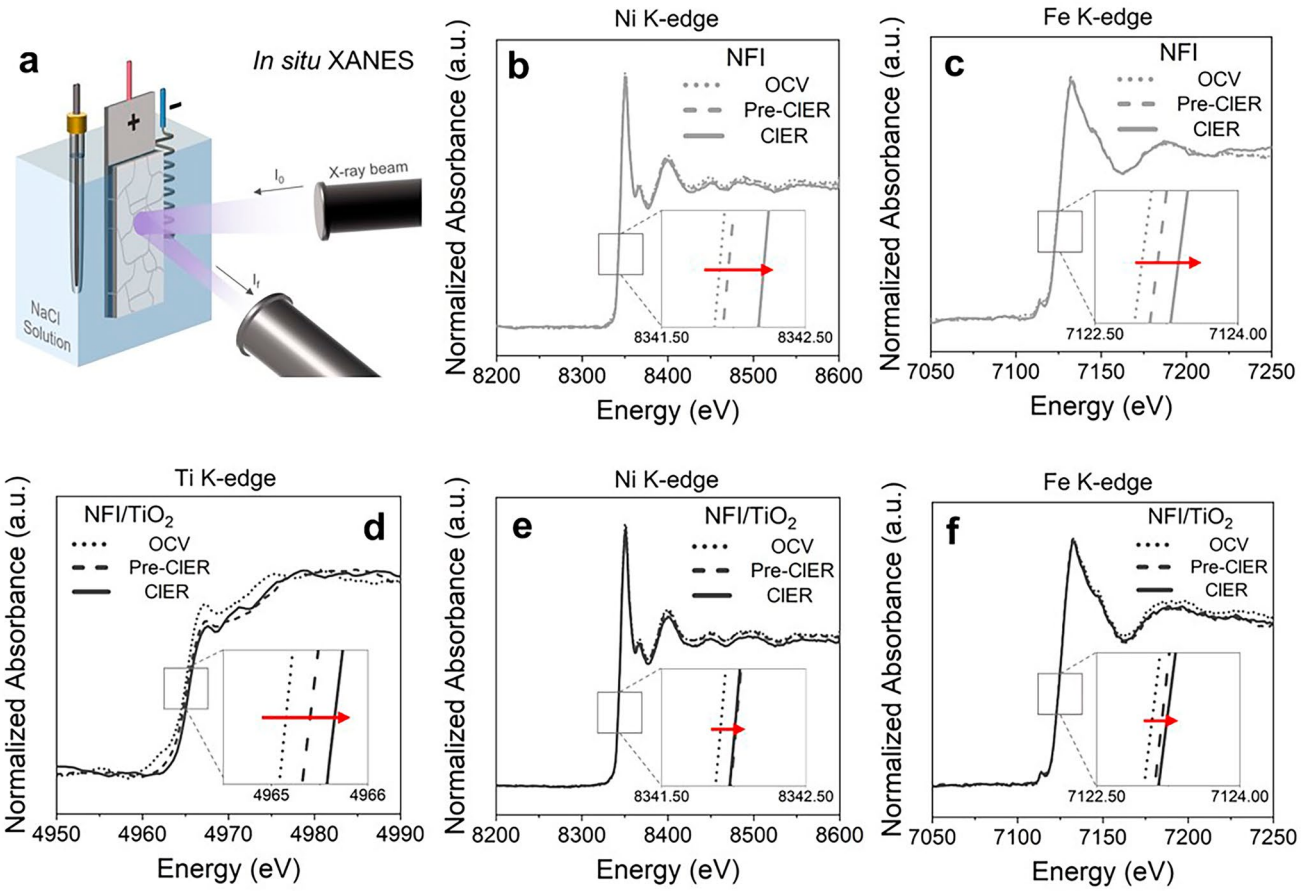

Fig. 3 The *operando* XANES analysis. **a** The schematic illustration of the setup. **b-c** Normalized XANES spectra in Ni K-edge and Fe K-edge for NFI. **d-f** Normalized XANES spectra in Ti K-edge, Ni K-edge, and Fe K-edge for NFI/TiO_2. The spectra were collected under OCV, pre-ClER at 1 mA cm^{-2}, and ClER at 3 mA cm^{-2} in 100 mM NaCl

$$NH_3 + HOCl \rightarrow NH_2Cl + H_2O \quad (8)$$

$$NH_2Cl + HOCl \rightarrow NHCl_2 + H_2O \quad (9)$$

$$NH_2Cl + NHCl_2 \rightarrow N_2 + 3H^+ + Cl^- \quad (10)$$

As shown in Fig. 4c, the NH_4^+ degradation rates were in the order of NFI/TiO_2 > BDD > IrO_2/TiO_2, in general agreement with the ClER activity. The metrics for BDD in 100 mM NaCl was quantified with CE_{ClER} of 61.5% and EE_{ClER} of 3.94 mmol Wh^{-1}. Furthermore, NFI/TiO_2 brought about comparable profiles for [TN] and [NH_4^+], whereas the TN decay rates were retarded for the others, more markedly for BDD (Fig. 4d) due to formation of nitrite ions (NO_2^-) measured up to 5 mM (Fig. S23). Formation of nitrate ions (NO_3^-) was always negligible in this experimental condition for all anodes. Albeit the BDD has been extensively deployed for water treatment owing to effective utilization of bound hydroxyl radical [55, 56], the mediated TN removal was incomplete due to the hydroxyl radical mediated oxidation to NO_2^- as a byproduct. The profiles of free/combined chlorine concentrations with NFI/TiO_2 (Fig. 4e) confirmed the breakpoint chlorination mechanism; a buildup of free chlorine initiated at ~ 2 h of electrolysis which extinguished NH_4^+. The stoichiometric NH_4^+-to-N_2 conversion by NFI/TiO_2 was additionally supported by almost consistent N balance by the sum of measured gaseous N_2, aqueous TN, and combined chlorine (Fig. 4f). In comparison, the [free chlorine] was in quasi-steady states for IrO_2/TiO_2 and BDD up to 3 h (Fig. S24), in compatible with the incomplete conversion of NH_4^+. The generation of oxynitrogen anions during the breakpoint chlorination could be invigorated by an elevation in relative RCS dosage

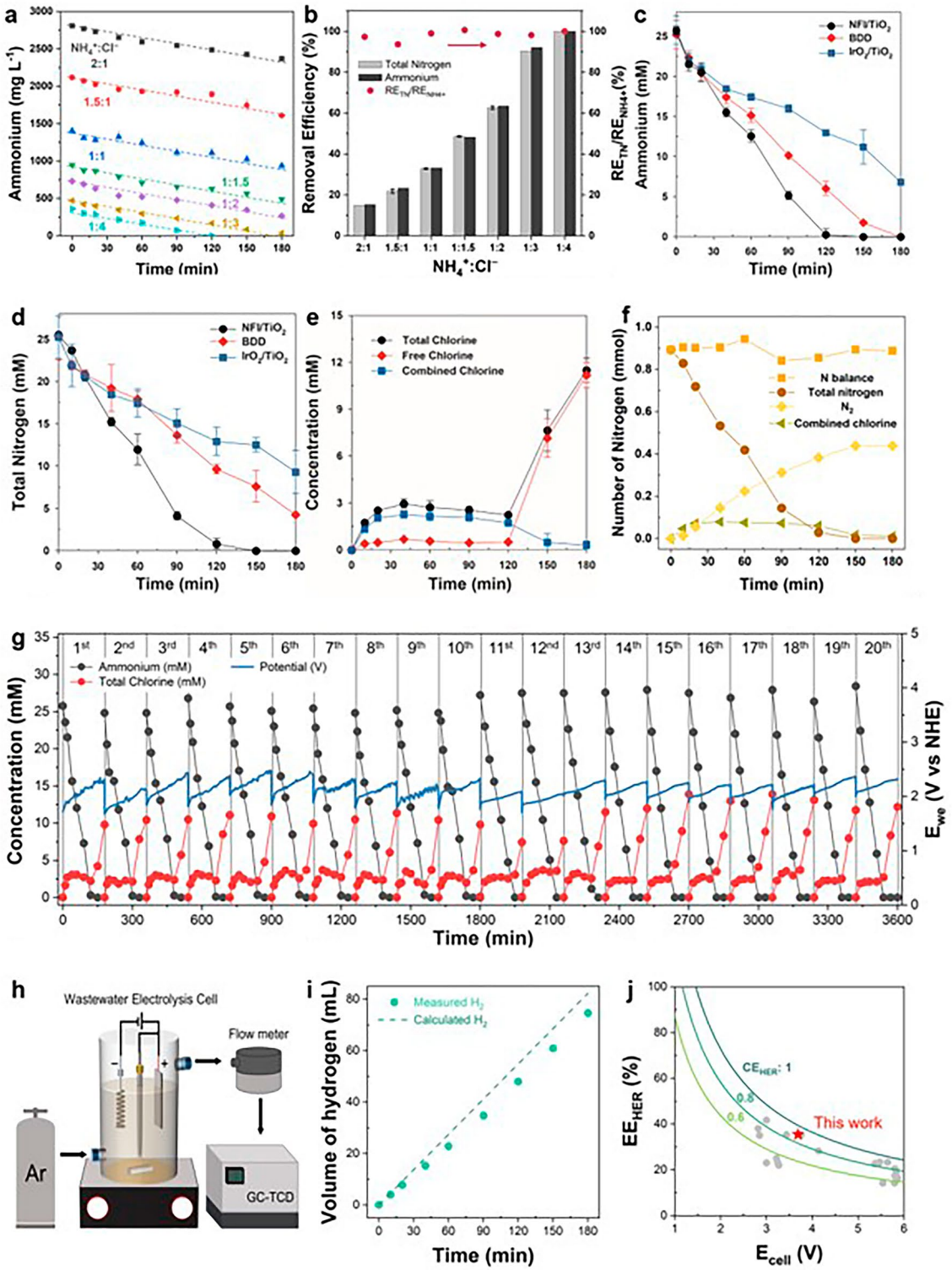

Fig. 4 RCS-mediated electrochemical deammonification coupled with H_2 production. **a-b** Concentration profiles of NH_4^+ and removal efficiency of TN and NH_4^+ for NFI/TiO_2 with variable $[NH_4^+]_0$ (25–200 mM). **c-d** Concentration profiles of NH_4^+ and TN for NFI/TiO_2 in comparison with BDD and IrO_2/TiO_2. **e–f** Concentration profiles of free, combined, and total chlorine with N balance calculated by the sum of TN, N_2 gas, and combined chlorine for NFI/TiO_2. **g** Repeated batch degradations of NH_4^+ with NFI/TiO_2. **h** Schematic illustration for H_2 quantification. **i-j** Metrics in terms of CE_{HER} and EE_{HER} in comparison with theoretical values (solid lines for CE_{HER} of 1, 0.8, and 0.6) and reported values in literature (gray circle) [15, 51–53]. Galvanostatic (30 mA cm^{-2}) electrolysis was performed with NH_4^+-laden synthetic wastewater ($[NH_4^+]_0 = 25$ mM for **c-j**, $[Cl^-]_0 = 100$ mM)

https://doi.org/10.1007/s40820-024-01542-x

[57]. Thus, intrinsically continuous and distributed feed of RCS in electrochemical chlorination would be beneficial for an ideal NH_4^+-to-N_2 conversion with minimal byproducts generation. As a confirmation, a batch injection of 100 mM of NaOCl (comparable with the total RCS generated by NFI/TiO_2 for 3 h) to the synthetic wastewater brought about rapid exhaustion of NH_4^+ within 15 min, but the TN decay was markedly retarded to be incomplete after 3 h. (Fig. S25). Consequently, the selective ClER on NFI/TiO_2 effectively led to more facile achievement of breakpoint than the benchmark anodes, while far lower steady-state [RCS] compared to a chemical chlorination prevented oxyanion byproducts (NO_2^- and NO_3^-) formation.

For all $[NH_4^+]_0$ conditions, the ultimate concentrations of $[NO_2^-]$ and $[NO_3^-]$ in electrolyte were negligible (Fig. S26) to maintain RE for [TN]/$[NH_4^+]$ near unity for NFI/TiO_2 (Fig. 4b). These observations suggested that the heterogeneous charge transfer (ClER) would be rate-limiting under our galvanostatic condition [16, 58], i.e., nucleophilic attack of RCS to NH_3 (Eq. 8) and chemical reactions among chloramines (Eqs. 9 and 10) were more facile than the ClER [16]. Regarding the mass balance of Cl, on the other hand, monotonic declines of $[Cl^-]$ was noted with an increasing rate as $[NH_4^+]_0$ decreased (Fig. S26). Since oxychlorine anions (e.g., ClO_3^- and ClO_4^-) were always negligible, likely owing to the low [RCS] before the breakpoint, the reduced $[Cl^-]$ would be ascribed to a volatilization of Cl_2 gas. The general CE of NH_4^+-to-N_2 conversion ($3e^-$ transfer) at $[NH_4^+]/[Cl^-]$ of 0.25 was 58.6% after 2 h of electrolysis (breakpoint as indicated by Fig. S27), being far lower than the CE_{ClER} measured in 0.1 M NaCl. However, the reduced $[Cl^-]$ accounted for CE of 43.8% (assuming $2e^-$ transfer to RCS) to roughly close the charge balance.

In order to confirm the stability of NFI/TiO_2 anode during the water treatment, the batch NH_4^+ degradation experiment was repeated up to 20 cycles (Fig. 4g). The efficacy of the RCS-mediated deammonification was maintained without a significant variation based on the pseudo zero-order rate constants of NH_4^+ abatement ranging from 11.1 to 12.8 mM h^{-1}.The typical profiles of total/free chlorine in breakpoint chlorination were consistently reproduced as well (Fig. S28). The anodic potential moderately increased within a cycle, which was ascribed to the reduced electrical conductivity by deammonification since it was recovered at the beginning of the subsequent cycle. After the sequencing batch cycles, the used NFI/TiO_2 retained crystalline integrity of spinel $NiFe_2O_4$ and anatase TiO_2 structure, as revealed by XRD (Fig. S29). We additionally performed XPS and Raman spectroscopy analyses on the used NFI/TiO_2 samples to evaluate the stability of the heterojunction anode. The analytical depth of XPS is typically 5–10 nm to target the surface [59]. As expected, the Ni and Fe 2*p* peaks in NFI/TiO_2 displayed significantly reduced intensities compared to those in NFI, which can be attributed to the limited amount of Ni and Fe that migrated to the surface owing to a thermal diffusion during the annealing (Fig. S30). Nevertheless, these peaks were well-preserved after the extended electrolysis (Fig. S31a, b). Furthermore, both photoelectron spectra and Raman spectra of NFI/TiO_2 before and after electrolysis reveals that the signals related to the TiO_2 outer layer were consistent after the electrolysis. (Figs. S31c and S32). Consequently, NFI/TiO_2 anode proved a long-term stability during electrolysis of wastewater with near-neutral pH.

Figure 4h illustrates the quantification method of H_2 generation from the undivided WEC with NFI/TiO_2 anode. Headspace of the gas-sealed reactor was connected to a flow meter, while the composition was measured by GC-TCD. Figure 4i presents the observed rate of H_2 production during the galvanostatic electrolysis of the synthetic wastewater. The current efficiency for HER is an important figure-of-merit, together with energy efficiency, in the wastewater electrolysis to compare the energy conversion reaction selectivity [12, 15]. The CE_{HER} ranged 85%–90% during the course of electrolysis, averaged to 85.8% (Fig. S33). A portion of passed charge unused for the HER could be dissipated by undesired reactions, such as reduction of combined chlorine, and oxyanions (*e.g.*, NO_x^-, ClO_x^-) on the Pt cathode, albeit quantification of individual side reaction was infeasible in the undivided cell. Concurrently, the EE_{HER} (representing the conversion efficiency of electric energy to H_2) was averaged to 35.4% during the operation at 30 mA cm^{-2}. The observed metrics for CE_{HER} and EE_{HER} outweighed prior reports ($CE_{HER} < 80\%$ and $EE_{HER} < 23\%$ at $j > 20$ mA cm^{-2}) regarding the wastewater electrolysis with IrO_2 based anodes and variable compositions of wastewater (Fig. 4j) [15, 51–53]. The produced gas mixture during the initial 2 h of electrolysis primarily consisted of 2.0 mmol H_2 (83%) and 0.44 mmol N_2 (17%).

The attenuated OER on the NFI/TiO_2 anode could lead to negligible oxygen reduction reaction, in-turn elevating the CE_{HER}. Gaseous $[O_2]$ in the reactor headspace was indeed below the detection limit. In addition, the facile quenching of RCS by NH_4^+ would minimize the chlorine reduction reaction;

i.e., RCS-mediated oxidation of electron donating pollutants allowed selective HER even in membrane-less configuration. Therefore, the quasi-absolute selectivity for ClER on NFI/TiO_2 could intensify the synergism in bifunctional WEC for water treatment coupled with H_2 generation. On the other hand, the CE_{HER} and E_{cell} exclusively determine the EE_{HER} (Fig. 4j) [15], while the voltage loss would be governed by the anodic η and ohmic resistance. Consequently, the admirable electrocatalytic ClER activity of NFI/TiO_2 also contributed to the enhanced EE_{HER}. It is worth mentioning that the marked EE_{HER} value in this study can be easily raised by lowering the E_c (j), which reduces the *iR* loss but inevitably retards the ClER and mediated pollutants removal. This apparent trade-off relations between the rate of pollutants removal and energy conversion efficiency have been noted previously [15], highlighting the importance of process engineering. In addition, the EE_{HER} can be escalated with an increasing electrical conductivity of wastewater, by mixing with seawater as an example, which deserves further research.

3.5 Scaled-Up Application for Toilet Wastewater Treatment

For demonstration of practical applicability, scaled-up NFI/TiO_2 anodes and electrolysis cell (effective volume of 10 L) were fabricated as shown in Fig. 5a. It should be mentioned that our straightforward dip coating and thermal decomposition methods for NFI/TiO_2 were amenable for the scaling. In order to avoid uneven coating and current distribution, multiple anodes were matched with commercial AISI 304 stainless steel cathodes in a sandwich module with total surface area of 0.286 m^2 (submerged area: 0.191 m^2). The cost-effectiveness and moderately efficient HER property could rationalize the deployment of stainless steel [15]. Figure 5b–e depicts the profiles of principal pollutants within a cycle of sequencing batch operation at galvanostatic condition of 52.5 A (27.5 mA cm^{-2}). The pilot WEC exhibited eminent removal efficiency for COD and turbidity, due to well-known reactivity of the electrolytic RCS toward organic compounds in wastewater. The EEM before and after treatment (Fig. S34) additionally showed evident reduction of humic-like substances in the DOM, as represented by the peak centered at 430/360 nm [60]. The influent NH_4^+ was completely eliminated within 20 min by the swift reactions with RCS, whereas the concurrent decline of [TN] became more sluggish after 20 min to demand ~ 2 h for full annihilation of TN. It was presumably because the chlorination of monochloramine to dichloramine (Eq. 9) was retarded due to competition for RCS with organic compounds and monochloramine. A formation of organic chloramines from chlorination of organic nitrogen species (e.g., protein) in wastewater could not be ruled out as well. The CE calculated for initial 20 min was 61.3% for COD oxidation and 26.9% for TN conversion, being comparable with CE_{ClER} measured in 0.1 M NaCl (86%). It corroborated that the exceptional ClER on NFI/TiO_2 was maintained in the scaled-up process. The total CE for pollutants oxidation in real wastewater exceeded the estimates for the synthetic one with NH_4^+ only, because more abundant organic electron donors minimized the volatilization of unreacted Cl_2. Additionally, our wastewater electrolysis cell with NFI/TiO_2 anode and toilet wastewater achieved superior energy efficiency for removal of COD, TN, and NH_4^+-N, compared to previous electrooxidation processes using precious metal-based anodes (Table S1).

The H_2 generation constitutes a crucial advantage of WEC for energy storage coupled with wastewater treatment, when powered by renewable energy sources. The importance of decentralized H_2 production to reduce carbon footprint has been demonstrated recently by a life cycle analysis, primarily owing to the reduced CO_2 generation from transportation [14]. Given ideal charge transfer and homogeneous transformation, degradation of unit mole of NH_3 (converting to 1/2 mol of N_2 with 3 e^- transfer) and Total organic carbon (TOC, converting to 1 mol of CO_2 with 8 e^- transfer) would produce 1.5 and 4 mol of H_2, respectively. Assuming a composition of latrine wastewater to be 20 mM TOC and 10 mM NH_4^+, the full mineralization and deammonification would generate a gas mixture with 79% H_2, 17% CO_2, and 4% N_2. This composition would be suitable for further conversion by ignition in internal combustion engine or boiler which would reduce volatilization of toxic chlorinated organic compounds ($C_xH_yCl_z$). However, the dependence on the wastewater matrix should be further investigated in a long-term operation study.

4 Conclusions

In summary, the NFI/TiO_2 anode is characterized as Ir-doped spinel $NiFe_2O_4$ in heterojunction with nanoporous anatase TiO_2 layer, with strong electronic interaction across

 https://doi.org/10.1007/s40820-024-01542-x

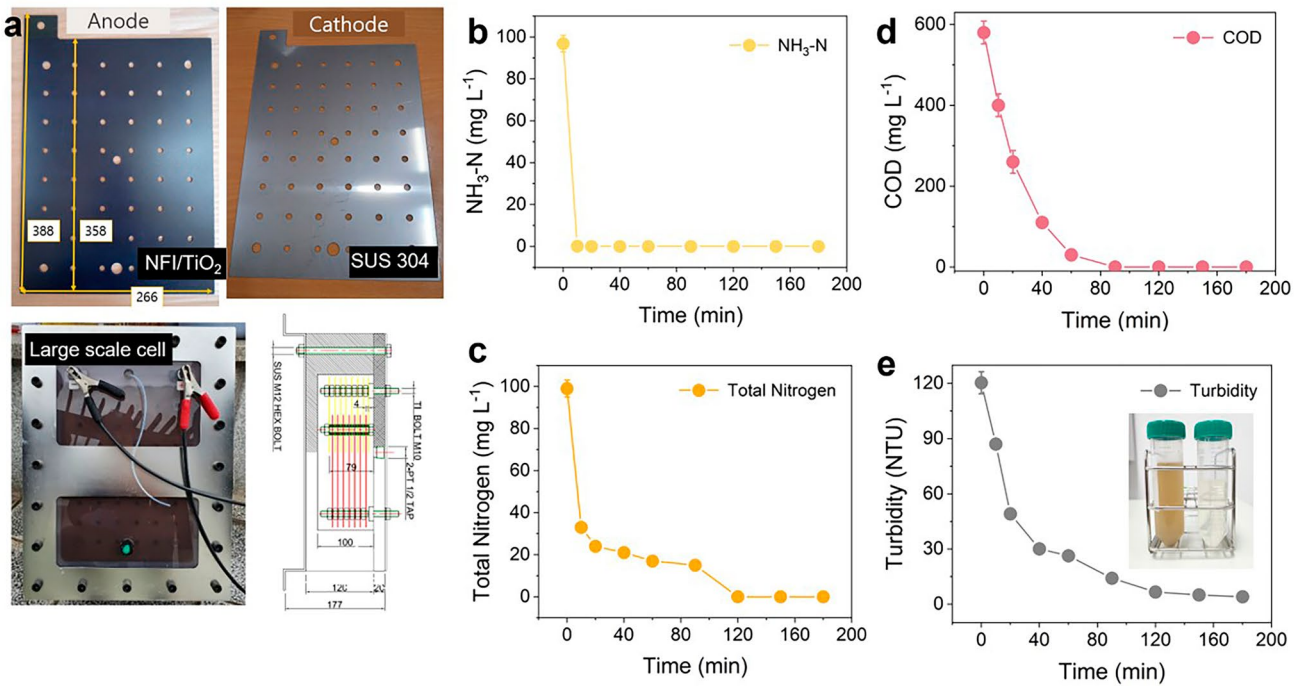

Fig. 5 Demonstration of a scaled-up WEC with toilet wastewater. **a** Scaled-up NFI/TiO_2 anode, stainless steel 304 cathode, and WEC (effective volume of 10 L) with a sandwich module. **b-e** Concentration profiles of NH_3-N, TN, COD, and turbidity. The inset in **e** shows photographs of influent (left) and effluent (right)

the junction. The tiny amounts of Ir bring about exceptional intrinsic activity of NFI both for OER (in KOH solutions) and ClER (in NaCl solutions), surpassing the benchmark IrO_2. The TiO_2 overlayer enhances the ClER selectivity and durability of NFI during ClER in near-neutral pH. The variation of ECSA, relation of CE_{ClER} with PZC, and the dynamic valency change during *in situ* XANES analysis demonstrated that the upper TiO_2 serves as the active ClER sites, while the underlying conductive NFI works as the ohmic contact. The charge withdrawing by NFI would facilitate the Cl-chemisorption on charge-deficient TiO_2. These synergisms allow selective and robust RCS generation on NFI/TiO_2 architecture, which in turn leads to facile degradation of aqueous pollutants as showcased with stoichiometric NH_4^+-to-N_2 conversion in NH_4^+-laden synthetic wastewater. In addition, the alleviated concentrations of dissolved oxygen and RCS can enhance the H_2 production in single-compartment WEC. The successful operation of scaled-up electrode module for electrolysis of toilet wastewater further substantiated the practical applicability of NFI/TiO_2. Consequently, NFI/TiO_2 would be a promising candidate for WEC as an option for on-site wastewater treatment and reuse, with decentralized H_2 production from nonconventional water sources.

Acknowledgements This work was financially supported by the National Research Foundation of Korea (NRF) grants (2022R1A2C4001228, 2022M3H4A4097524, 2022M3I3A1082499, and 2021M3I3A1084818), and the Technology Innovation Program (20026415) of the Ministry of Trade, Industry & Energy (MOTIE, Korea). The authors also acknowledge the supports from Nanopac for fabrication of scaled-up reactor.

Author Contributions Sukhwa Hong performed writing—original, visualization, methodology, and validation. Jiseon Kim presented formal analysis, investigation, and validation. Jaebeom Park contributed formal analysis and investigation. Sunmi Im conducted formal analysis and investigation. Michael R. Hoffmann provided resources and conceptualization. Kangwoo Cho carried out supervision, writing—review & editing, project administration, funding acquisition, and conceptualization.

Declarations

Conflict of Interest The authors declare that they have no known competing financial interests of personal relationships that could have appeared to influence the work reported in this paper.

Supplementary Information The online version contains supplementary material available at https://doi.org/10.1007/s40820-024-01542-x.

References

1. L. Sun, H. Dong, Y. Lu, L. Zhang, L. Yang et al., A hydrate-based zero liquid discharge method for high-concentration organic wastewater: resource recovery and water reclamation. npj Clean Water **6**, 49 (2023). https://doi.org/10.1038/s41545-023-00262-w
2. S. Grego, The humble toilet is an opportunity for sustainable water reuse. Nat. Water **1**, 900–901 (2023). https://doi.org/10.1038/s44221-023-00154-w
3. H. Feng, J. Yu, J. Tang, L. Tang, Y. Liu et al., Enhanced electro-oxidation performance of FeCoLDH to organic pollutants using hydrophilic structure. J. Hazard. Mater. **430**, 128464 (2022). https://doi.org/10.1016/j.jhazmat.2022.128464
4. C.A. Cid, F. Abiola, M. Starkl, Can international nonsewered sanitation standards help solve the global sanitation crisis? Environ. Sci. Technol. **56**, 699–706 (2022). https://doi.org/10.1021/acs.est.1c03471
5. S. Pei, S. You, J. Ma, X. Chen, N. Ren, Electron spin resonance evidence for electro-generated hydroxyl radicals. Environ. Sci. Technol. **54**, 13333–13343 (2020). https://doi.org/10.1021/acs.est.0c05287
6. P. Subramani, M. Basil, P. Rosario, D.R. Jalaja, V. Choudhary et al., Water recycling public toilets based on onsite electrochemical wastewater treatment. Environ. Sci.: Water Res. Technol. **10**, 157–167 (2024). https://doi.org/10.1039/d3ew00454f
7. K. Cho, M.R. Hoffmann, $Bi_xTi_{1-x}O_z$ functionalized heterojunction anode with an enhanced reactive chlorine generation efficiency in dilute aqueous solutions. Chem. Mater. **27**, 2224–2233 (2015). https://doi.org/10.1021/acs.chemmater.5b00376
8. S. Hong, T.-K. Lee, M.R. Hoffmann, K. Cho, Enhanced chlorine evolution from dimensionally stable anode by heterojunction with Ti and Bi based mixed metal oxide layers prepared from nanoparticle slurry. J. Catal. **389**, 1–8 (2020). https://doi.org/10.1016/j.jcat.2020.04.009
9. K. Cho, Y. Qu, D. Kwon, H. Zhang, C.A. Cid et al., Effects of anodic potential and chloride ion on overall reactivity in electrochemical reactors designed for solar-powered wastewater treatment. Environ. Sci. Technol. **48**, 2377–2384 (2014). https://doi.org/10.1021/es404137u
10. C. Zhang, D. He, J. Ma, T.D. Waite, Active chlorine mediated ammonia oxidation revisited: reaction mechanism, kinetic modelling and implications. Water Res. **145**, 220–230 (2018). https://doi.org/10.1016/j.watres.2018.08.025
11. Y. Ji, J. Bai, J. Li, T. Luo, L. Qiao et al., Highly selective transformation of ammonia nitrogen to N_2 based on a novel solar-driven photoelectrocatalytic-chlorine radical reactions system. Water Res. **125**, 512–519 (2017). https://doi.org/10.1016/j.watres.2017.08.053
12. S. Hong, G. Choi, N. Thi Yen Phan, H. Shin, J. Lim, Efficient and durable iridium-doped SnO_2 anode for reactive chlorine species-mediated urine wastewater treatment. Chem. Eng. J. **493**, 152698 (2024). https://doi.org/10.1016/j.cej.2024.152698
13. C.E. Adams, Removing nitrogen from waste water. Environ. Sci. Technol. **7**, 696–701 (1973). https://doi.org/10.1021/es60080a006
14. L.R. Winter, N.J. Cooper, B. Lee, S.K. Patel, L. Wang et al., Mining nontraditional water sources for a distributed hydrogen economy. Environ. Sci. Technol. **56**, 10577–10585 (2022). https://doi.org/10.1021/acs.est.2c02439
15. K. Cho, M.R. Hoffmann, Molecular hydrogen production from wastewater electrolysis cell with multi-junction BiO_x/TiO_2 anode and stainless steel cathode: current and energy efficiency. Appl. Catal. B Environ. **202**, 671–682 (2017). https://doi.org/10.1016/j.apcatb.2016.09.067
16. Y. Liu, L. Li, R. Goel, Kinetic study of electrolytic ammonia removal using Ti/IrO_2 as anode under different experimental conditions. J. Hazard. Mater. **167**, 959–965 (2009). https://doi.org/10.1016/j.jhazmat.2009.01.082
17. L. Ding, K. Li, W. Wang, Z. Xie, S. Yu et al., Amorphous iridium oxide-integrated anode electrodes with ultrahigh material utilization for hydrogen production at industrial current densities. Nano-Micro Lett. **16**, 203 (2024). https://doi.org/10.1007/s40820-024-01411-7
18. E. Lacasa, J. Llanos, P. Cañizares, M.A. Rodrigo, Electrochemical denitrificacion with chlorides using DSA and BDD anodes. Chem. Eng. J. **184**, 66–71 (2012). https://doi.org/10.1016/j.cej.2011.12.090
19. Y.-Y. Yang, H.-P. Feng, X.-G. Zhang, H. Guo, X.-J. Wen et al., Regulating and protecting of oxygen vacancy endow MoO_{3-x}@$Zn_2In_2S_5$ S-scheme core–shell heterojunction with high-efficiency organic pollutant removal and bacterial disinfection: correlation of pollutant active sites to degradation pathways. Chem. Eng. J. **490**, 151309 (2024). https://doi.org/10.1016/j.cej.2024.151309
20. H. Feng, J. Yu, L. Tang, J. Wang, H. Dong et al., Improved hydrogen evolution activity of layered double hydroxide by optimizing the electronic structure. Appl. Catal. B Environ.

297, 120478 (2021). https://doi.org/10.1016/j.apcatb.2021.120478

21. Y.-Y. Yang, H. Guo, D.-W. Huang, L. Li, H.-Y. Liu et al., Simultaneously tuning oxygen reduction pathway and charge transfer dynamics toward sacrificial agent-free photocatalytic H_2O_2 production for *in situ* water disinfection. Chem. Eng. J. **479**, 147863 (2024). https://doi.org/10.1016/j.cej.2023.147863
22. J. Kim, M.-C. Kim, S.S. Han, K. Cho, Accessible Ni-Fe-oxalate framework for electrochemical urea oxidation with radically enhanced kinetics. Adv. Funct. Mater. **34**, 2315625 (2024). https://doi.org/10.1002/adfm.202315625
23. M. Ning, Y. Wang, L. Wu, L. Yang, Z. Chen et al., Hierarchical interconnected NiMoN with large specific surface area and high mechanical strength for efficient and stable alkaline water/seawater hydrogen evolution. Nano-Micro Lett. **15**, 157 (2023). https://doi.org/10.1007/s40820-023-01129-y
24. L. Jiang, J. Pan, Q. Li, H. Chen, S. Zhou et al., A holistic green system coupling hydrogen production with wastewater valorisation. EcoMat **4**, e12254 (2022). https://doi.org/10.1002/eom2.12254
25. S. Hong, K. Ham, J. Hwang, S. Kang, M.H. Seo et al., Active motif change of Ni-Fe spinel oxide by Ir doping for highly durable and facile oxygen evolution reaction. Adv. Funct. Mater. **33**, 2209543 (2023). https://doi.org/10.1002/adfm.202209543
26. E. Rahman, S. Hong, J. Lee, S.W. Hong, K. Cho, Ni-Fe oxides/TiO_2 heterojunction anodes for reactive chlorine generation and mediated water treatment. ACS Appl. Mater. Interfaces **15**, 17867–17878 (2023). https://doi.org/10.1021/acsami.3c00581
27. S. Kim, S. Choung, W. Lee, S. Bae, J.W. Han et al., Tuning electrochemical water oxidation towards ozone evolution with heterojunction anode architectures. J. Mater. Chem. A **10**, 17132–17141 (2022). https://doi.org/10.1039/D2TA02731C
28. M.S. Koo, K. Cho, J. Yoon, W. Choi, Photoelectrochemical degradation of organic compounds coupled with molecular hydrogen generation using electrochromic TiO_2 nanotube arrays. Environ. Sci. Technol. **51**, 6590–6598 (2017). https://doi.org/10.1021/acs.est.7b00774
29. J. Lim, Y. Yang, M.R. Hoffmann, Activation of peroxymonosulfate by oxygen vacancies-enriched cobalt-doped black TiO_2 nanotubes for the removal of organic pollutants. Environ. Sci. Technol. **53**, 6972–6980 (2019). https://doi.org/10.1021/acs.est.9b01449
30. Y.U. Shin, H.Y. Yoo, S. Kim, K.M. Chung, Y.G. Park et al., Sequential combination of electro-Fenton and electrochemical chlorination processes for the treatment of anaerobically-digested food wastewater. Environ. Sci. Technol. **51**, 10700–10710 (2017). https://doi.org/10.1021/acs.est.7b02018
31. B.M. De Borba, R.F. Jack, J.S. Rohrer, J. Wirt, D. Wang, Simultaneous determination of total nitrogen and total phosphorus in environmental waters using alkaline persulfate digestion and ion chromatography. J. Chromatogr. A **1369**, 131–137 (2014). https://doi.org/10.1016/j.chroma.2014.10.027
32. Q. Emparan, R. Harun, J.A. Kodiappan, Effect of microalgae-to-palm oil mill effluent (POME) ratio for rapid effective pollutants removal and biomass production. Desalin. Water Treat. **198**, 119–125 (2020). https://doi.org/10.5004/dwt.2020.25979
33. I. Vyrides, D.C. Stuckey, A modified method for the determination of chemical oxygen demand (COD) for samples with high salinity and low organics. Bioresour. Technol. **100**, 979–982 (2009). https://doi.org/10.1016/j.biortech.2008.06.038
34. A. Ahlawat, V.G. Sathe, V.R. Reddy, A. Gupta, Mossbauer, Raman and X-ray diffraction studies of superparamagnetic $NiFe_2O_4$ nanoparticles prepared by sol–gel auto-combustion method. J. Magn. Magn. Mater. **323**, 2049–2054 (2011). https://doi.org/10.1016/j.jmmm.2011.03.017
35. H. Li, S. Chen, Y. Zhang, Q. Zhang, X. Jia et al., Systematic design of superaerophobic nanotube-array electrode comprised of transition-metal sulfides for overall water splitting. Nat. Commun. **9**, 2452 (2018). https://doi.org/10.1038/s41467-018-04888-0
36. G. Dong, M. Fang, J. Zhang, R. Wei, L. Shu et al., *In situ* formation of highly active Ni–Fe based oxygen-evolving electrocatalysts *via* simple reactive dip-coating. J. Mater. Chem. A **5**, 11009–11015 (2017). https://doi.org/10.1039/C7TA01134B
37. Q. Xue, H.-Y. Sun, Y.-N. Li, M.-J. Zhong, F.-M. Li et al., Au@Ir core-shell nanowires towards oxygen reduction reaction. Chem. Eng. J. **421**, 129760 (2021). https://doi.org/10.1016/j.cej.2021.129760
38. K.S. Exner, T. Lim, S.H. Joo, Circumventing the OCl versus OOH scaling relation in the chlorine evolution reaction: beyond dimensionally stable anodes. Curr. Opin. Electrochem. **34**, 100979 (2022). https://doi.org/10.1016/j.coelec.2022.100979
39. C. Mahala, M.D. Sharma, M. Basu, 2D nanostructures of $CoFe_2O_4$ and $NiFe_2O_4$: efficient oxygen evolution catalyst. Electrochim. Acta **273**, 462–473 (2018). https://doi.org/10.1016/j.electacta.2018.04.079
40. Z.-G. Ye, H.-M. Meng, D.-B. Sun, Electrochemical impedance spectroscopic (EIS) investigation of the oxygen evolution reaction mechanism of Ti/IrO_2 +MnO_2 electrodes in 0.5m H_2SO_4 solution. J. Electroanal. Chem. **621**, 49–54 (2008). https://doi.org/10.1016/j.jelechem.2008.04.009
41. D.H. Taffa, R. Dillert, A.C. Ulpe, K.C.L. Bauerfeind, T. Bredow et al., Photoelectrochemical and theoretical investigations of spinel type ferrites ($M_xFe_{3-x}O_4$) for water splitting: a mini-review. J. Photon. Energy **7**, 012009 (2017). https://doi.org/10.1117/1.jpe.7.012009
42. G. Rekhila, Y. Bessekhouad, M. Trari, Visible light hydrogen production on the novel ferrite $NiFe_2O_4$. Int. J. Hydrog. Energy **38**, 6335–6343 (2013). https://doi.org/10.1016/j.ijhydene.2013.03.087
43. K. Kitsuka, K. Kaneda, M. Ikematsu, M. Iseki, K. Mushiake et al., N-type TiO_2 thin films for electrochemical ozone production. J. Electrochem. Soc. **157**, F30 (2010). https://doi.org/10.1149/1.3265469
44. I.A. Moreno-Hernandez, B.S. Brunschwig, N.S. Lewis, Crystalline nickel, cobalt, and manganese antimonates as

electrocatalysts for the chlorine evolution reaction. Energy Environ. Sci. **12**, 1241–1248 (2019). https://doi.org/10.1039/C8EE03676D

45. S. Virtanen, P. Schmuki, A.J. Davenport, C.M. Vitus, Dissolution of thin iron oxide films used as models for iron passive films studied by *in situ* X-ray absorption near-edge spectroscopy. J. Electrochem. Soc. **144**, 198–204 (1997). https://doi.org/10.1149/1.1837385
46. J. Kunze, A. Ghicov, H. Hildebrand, J.M. Macak, L. Traveira et al., Challenges in the surface analytical characterisation of anodic TiO_2 films–a review. Z. Für Phys. Chem. **219**, 1561–1582 (2005). https://doi.org/10.1524/zpch.2005.219.11.1561
47. C.E. Finke, S.T. Omelchenko, J.T. Jasper, M.F. Lichterman, C.G. Read et al., Enhancing the activity of oxygen-evolution and chlorine-evolution electrocatalysts by atomic layer deposition of TiO_2. Energy Environ. Sci. **12**, 358–365 (2019). https://doi.org/10.1039/c8ee02351d
48. S.R. Kelly, H.H. Heenen, N. Govindarajan, K. Chan, J.K. Nørskov, OH binding energy as a universal descriptor of the potential of zero charge on transition metal surfaces. J. Phys. Chem. C **126**, 5521–5528 (2022). https://doi.org/10.1021/acs.jpcc.1c10362
49. J. Park, E.J. Hwang, S. Hong, K. Cho, Electrochemical chlorine evolution by Bi–Ti oxide with a heterojunction on Ir–Ta oxide: insights from the effects of layer configurations. J. Phys. Chem. C **127**, 9640–9649 (2023). https://doi.org/10.1021/acs.jpcc.3c01841
50. K. Ham, S. Hong, S. Kang, K. Cho, J. Lee, Extensive active-site formation in trirutile $CoSb_2O_6$ by oxygen vacancy for oxygen evolution reaction in anion exchange membrane water splitting. ACS Energy Lett. **6**, 364–370 (2021). https://doi.org/10.1021/acsenergylett.0c02359
51. J. Kim, D. Kwon, K. Kim, M.R. Hoffmann, Electrochemical production of hydrogen coupled with the oxidation of arsenite. Environ. Sci. Technol. **48**, 2059–2066 (2014). https://doi.org/10.1021/es4046814
52. J. Choi, Y. Qu, M.R. Hoffmann, SnO_2, IrO_2, Ta_2O_5, Bi_2O_3, and TiO_2 nanoparticle anodes: electrochemical oxidation coupled with the cathodic reduction of water to yield molecular H_2, in *Nanotechnology for Sustainable Development*. ed. by M.S. Diallo, N.A. Fromer, M.S. Jhon (Springer International Publishing, Cham, 2012), pp.223–234
53. H. Park, K.-H. Choo, H.-S. Park, J. Choi, M.R. Hoffmann, Electrochemical oxidation and microfiltration of municipal wastewater with simultaneous hydrogen production: influence of organic and particulate matter. Chem. Eng. J. **215**, 802–810 (2013). https://doi.org/10.1016/j.cej.2012.11.075
54. L. Li, Y. Liu, Ammonia removal in electrochemical oxidation: mechanism and pseudo-kinetics. J. Hazard. Mater. **161**, 1010–1016 (2009). https://doi.org/10.1016/j.jhazmat.2008.04.047
55. V. Schmalz, T. Dittmar, D. Haaken, E. Worch, Electrochemical disinfection of biologically treated wastewater from small treatment systems by using boron-doped diamond (BDD) electrodes: contribution for direct reuse of domestic wastewater. Water Res. **43**, 5260–5266 (2009). https://doi.org/10.1016/j.watres.2009.08.036
56. S.O. Ganiyu, C.A. Martínez-Huitle, Nature, mechanisms and reactivity of electrogenerated reactive species at thin-film boron-doped diamond (BDD) electrodes during electrochemical wastewater treatment. ChemElectroChem **6**, 2379–2392 (2019). https://doi.org/10.1002/celc.201900159
57. T.A. Pressley, D.F. Bishop, S.G. Roan, Ammonia-nitrogen removal by breakpoint chlorination. Environ. Sci. Technol. **6**, 622–628 (1972). https://doi.org/10.1021/es60066a006
58. A. Urtiaga, I. Ortiz, A. Anglada, D. Mantzavinos, E. Diamadopoulos, Kinetic modeling of the electrochemical removal of ammonium and COD from landfill leachates. J. Appl. Electrochem. **42**, 779–786 (2012). https://doi.org/10.1007/s10800-012-0458-5
59. C. Oliveira, C.R. Chaves, P. Bargiela, M. da Graça Carneiro da Rocha, A.F. da Silva et al., Surface studies of the chemical environment in gold nanorods supported by X-ray photoelectron spectroscopy (XPS) and *ab initio* calculations. J. Mater. Res. Technol. **15**, 768–776 (2021). https://doi.org/10.1016/j.jmrt.2021.08.059
60. M. Sgroi, P. Roccaro, G.V. Korshin, V. Greco, S. Sciuto et al., Use of fluorescence EEM to monitor the removal of emerging contaminants in full scale wastewater treatment plants. J. Hazard. Mater. **323**, 367–376 (2017). https://doi.org/10.1016/j.jhazmat.2016.05.035

 https://doi.org/10.1007/s40820-024-01542-x